Nature Communications

https://doi.org/10.1038/s41467-026-69926-8

Article in Press

Solid-liquid interface synthesis of selective (111)-oriented $Cs_2AgBiBr_6$ perovskite crystals

Received: 9 July 2025

Accepted: 9 February 2026

Cite this article as: Hong, E., Li, Z., Deng, M. *et al.* Solid-liquid interface synthesis of selective (111)-oriented $Cs_2AgBiBr_6$ perovskite crystals. *Nat Commun* (2026). https://doi.org/10.1038/s41467-026-69926-8

Enliu Hong, Ziqing Li, Ming Deng, Limin Wu & Xiaosheng Fang

Solid-liquid interface synthesis of selective (111)-oriented $Cs_2AgBiBr_6$ perovskite crystals

Enliu Hong[1], Ziqing Li[2]*, Ming Deng[1], Limin Wu[1,3]*& Xiaosheng Fang[1]*

[1]College of Smart Materials and Future Energy, State Key Laboratory of Molecular Engineering of Polymers, Fudan University, Shanghai 200433, P. R. China

[2]Shanghai Frontiers Science Research Base of Intelligent Optoelectronics and Perception, State Key Laboratory of Photovoltaic Science and Technology, College of Future Information Technology, Institute of Optoelectronics, Fudan University, Shanghai 200433, P. R. China

[3]College of Chemistry and Chemical Engineering, Inner Mongolia University, Hohhot 010021, P. R. China

* Corresponding author. Email: lzq@fudan.edu.cn; lmw@fudan.edu.cn, xshfang@fudan.edu.cn

Abstract

Achieving the preferred orientation of specific facets is crucial for regulating the anisotropic physical properties of crystal materials and optimizing the performance of semiconductor optoelectronic devices. However, the intrinsic challenges lie in precisely controlling the growth kinetics of crystal facets and suppressing defects during the spontaneous crystallization processes. Herein, we report the microdroplet interface synthesis of $Cs_2AgBiBr_6$ single crystals with controlled orientations. By selectively reducing the nucleation barrier of (111) facets via modulation of the solid-liquid interface energy, the random (100)/(110)/(111) orientations are transformed into a ~~highly~~ selective (111)-preferred orientation. Further, thermal annealing is demonstrated to effectively improve crystal quality by releasing lattice strain and

promoting octahedral reordering. Both theoretical calculations and experiments validate the advantages of (111)-oriented facets with higher ionic migrate energy and lower defect density than (100) and (110) facets, which result in better endurance to moisture and light irradiation. Besides, photodetectors based on the (111) facets exhibit superior performance to (100) and (110) facets. This work highlights the crucial role of interface energy in directing crystallographic orientation, providing theoretical basis and design strategies for the precise manipulation of crystal facets.

Keywords: interface synthesis, $Cs_2AgBiBr_6$ single crystals, (111)-preferred orientation, thermal annealing, photodetectors

Introduction

Solution-grown perovskite single crystals (PSCs) have fascinated the research community owning to their excellent optoelectronic properties in recent years[1,2]. However, the toxicity and stability issues of traditional lead-based PSCs still seriously restrict their commercialization process[3,4]. Lead-free double PSCs $A_2BB'X_6$ (A: Cs^+, Rb^+; X: Cl^-, Br^-, I^-), which replace lead with an environmentally friendly combination of monovalent (B: Ag^+, Na^+, etc.) and trivalent (B': In^{3+}, Bi^{3+}, Sb^{3+}, etc.) metal cations, can fundamentally address these challenges[5]. Specially, the unique alternating $[BX_6]^{5-}$ and $[B'X_6]^{3-}$ octahedral structures in double perovskites further enhance lattice rigidity and stability, thus providing a competitive platform for designing optoelectronic devices such as efficient and stable solar cells[6], sensitive photodetectors[7], and radiation sensors[8].

Solution processability of PSCs is a key advantage for fabricating low-cost large-area optoelectronic devices[9-12], but their practical applications are still limited by challenges in precursor stability, crystallization dynamics control and homogeneity assurance[13-15]. During the spontaneous crystallization process of PSCs, crystals can develop polyhedral shapes composed of planes with different orientations.

As the direct medium to interact with external environment, crystal facets play a crucial role in determining the physical properties of PSCs, as well as the paths and efficiency of chemical reactions[16-18]. By directional exposure or modification of specific crystal facets, on-demand design of desired functions can be achieved[19-21]. For example, the (111) facet of wide-bandgap perovskites was verified to own higher ion-migration activation energy and lower diffusion constant than the (100) facet, which was reported to significantly improve the operational stability of devices[22,23]. According to Wulff construction theory, the shape of the crystal in equilibrium state is determined by the sum of surface energy of each crystal facet[24], which means the crystal facets with lower surface energy are easier to be formed. From the perspective of thermodynamic, although the (111) facet exhibits lower surface energy than (110) and (100) facets since they are classified as a close-packed atomic arrangement, it's still a challenge to obtain high-quality PSCs with a preferred orientation particularly dominated by (111) facets. Because the formation of specific crystal facets is also affected by many other complex factors including temperature, solvent, additives, interface energy and so on[25-27].

In this work, we present the microdroplet interface synthesis of high-quality lead-free $Cs_2AgBiBr_6$ (CABB) PSCs with controlled orientation. To overcome the problems of polycrystalline agglomeration and random orientation in conventional solution methods, the crystal nuclei are induced to grow preferentially in a specific direction by regulating the nucleation barriers through the solid-liquid interface energy. This approach enables the transformation of CABB PSCs from random orientations composed of (100)/(110)/(111) facets to a ~~highly~~ selective orientation of (111) facets. The (111) facets are experimentally confirmed to exhibit much more suppressed phase segregation compared to that of (100) and (110) facets, which is due to the higher ion migration energy and vacancy formation energy as verified

by theoretical calculations at the same time. Moreover, the (111) facets also demonstrate minimal radiative recombination and exceptional optoelectronic performance. The understanding of the orientation-controlled mechanisms of CABB PSCs provides insights for selectively growing specific crystallographic facets, promoting the conversion from random growth to on-demand design.

Results and discussion

Crystal orientation and uniformity control are realized through interface energy regulation. Establishing optimal growth parameters is crucial for ensuring the solute atoms can be orderly incorporate into the lattice and minimize defects. Fig. 1a shows the interface synthesis process of CABB PSCs, which typically involves two procedures: slow evaporation (60 ℃) and high-temperature annealing (200 ℃). Such a growing condition creates a kinetic sweet spot where solute atoms orderly assemble into low-defect lattices, fulfilling the objectives of scalable production and device-grade crystallinity. The crystal structure of CABB is displayed in Fig. 1b, where alternating $[AgBr_6]^{5-}$ and $[BiBr_6]^{3-}$ double octahedron form the framework, with Cs^+ occupying the interstitial voids. During crystal growth, the solvent volatilization rate affects the supersaturation of the solution. Excessive solution supersaturation will result in rapid nucleation to form polycrystals or defects. Slow evaporation keeps the solution supersaturation low, giving the crystals enough time to grow in equilibrium to form larger and more complete PSCs. Near the equilibrium point, the monomers (ions, atoms and molecules) orderly aggregate to form single crystals through a self-assembly process[28]. The intrinsic challenge of synthesizing high-quality PSCs and further constructing high-performance devices lies in overcoming the issue of random orientation. As shown in Fig. 1c, Supplementary Fig. 1 and Supplementary Table 1, the atomic arrangements of (100)/(110)/(111) facets in CABB with a face-centered cubic structure demonstrate significant distinctions. The (111) facet

exhibits the most densely-packed characteristic. According to classical nucleation theory (Fig. 1g), the denser (111) facet possesses the lowest nucleation barrier because of lower surface energy than (100) and (110) facets, thus should have priority for growth. However, experimental results (Fig. 1d) reveal that uncontrolled nucleation on commonly-used Si/SiO_2 substrate (control group) leads to random orientations of (100)/(110)/(111) facets, evidenced by the coexistence of all three X-ray diffraction (XRD) signals (Fig. 1f). In contrast, employing a high-interface-energy PDMS substrate (target group) effectively aligns the nucleation preference exclusively toward the (111) facets, as confirmed by the absence of {110} signals in the XRD pattern. Specifically, the target group only reveals signals from {111} peaks at 13.6°, 27.4°, 41.6°, 56.5°. The full-width at half-maximum (FWHM) of the strongest peak reaches ultra-narrow 0.04°, indicating the high crystallinity of the as-prepared CABB PSCs. Additionally, the composition of CABB is confirmed by XPS spectra (Supplementary Fig. 2). The morphology and corresponding elemental distributions of three kinds of facets are shown in Fig. 1e and Supplementary Fig. 3, from which the regular shapes with clean surfaces and uniform dispersion of Cs, Ag, Bi, Br elements can be clearly seen. Density functional theory (DFT) calculations are applied to determine the ion migration energies of Ag^+ on the (100), (110) and (111) facets. The DFT results indicate that the (111) facet has the highest ion migration energy of ~3.5 eV, and the (100) facet is the easiest to migration (Fig. 1h). Besides, the (111) facet demonstrates superior stability to other orientations (Supplementary Fig. 4). Under the same storage conditions, the XRD intensities of {100} and {110} facets decayed significantly with time and disappeared completely by 80 days, leaving only {111} signals left after 80 days of ambient exposure. The target group maintained sharp {111} XRD peaks without peak shifting or broadening even after 80 days, with almost negligible surface degradation under moisture and oxygen attacks. This enhanced

stability stems from the enhanced water resistance and suppressed ion migration pathways in the (111)-oriented crystals. Beyond crystal orientations control, the deterministic tuning of crystal size and quantity can also be achieved by regulating the solution concentration and solvent evaporation rate (detailed in Supplementary Fig. 5 and Supplementary Fig. 6). Besides, this strategy exhibits exceptional reproducibility and is readily scalable with an actual yield of ~94.2%. These intriguing findings provide a facile strategy to synthesize highly-stable (111)-preferred orientated PSCs for optoelectronic applications.

In previous reports, it's generally acknowledged that using hydrophilic substrates with good wettability is necessary to acquire large-area homogeneous films[14,29]. In order to expose (111) facets as much as possible, it's widely used to incorporate specific additives to modify the solvent environment[30]. Nevertheless, the introduce of additives undoubtedly increases the cost and process complexity. Here, we develop a interface engineering strategy using hydrophobic substrates with high solid-liquid interface energy to obtain (111) facets, eliminating the need of additive-induced solvent modulation. Firstly, the role of substrate interface energy in regulating facet proportions of CABB crystals is experimentally revealed. Fig. 2a presents the two distinct crystal growth scenarios on substrates with different interface energy. Under low solid-liquid interface energy conditions, all facets, including (100), (110) and (111) will precipitate without selectivity. In contrast, when the interfacial energy is high, only the (111) facets are capable of growing on the substrates. As demonstrated in Figs. 2b−d, CABB crystals grown on substrates with ascending surface energies (pristine Si/SiO_2, treated Si/SiO_2, and PDMS) exhibit a progressive dominance of the (111) facet, increasing from ~ 45% to ~ 79% and finally reaching 100%. Statistical data (Figs. 2e-g) further confirm this trend: untreated Si/SiO_2 (contact angle ~ 38.7°) yields

random orientations of (100), (110), and (111) facets. In contrast, hydrophobic-treated Si/SiO_2 (contact angle ~ 62.6°) elevates the (111) facet proportion to ~75%. And PDMS (contact angle ~ 114.5°) substrate achieves exclusive (111) orientation. The concrete statistical data are provided in Supplementary Table 2, which clearly reveal the trend of the crystal facet proportions related to substrates. This correlation between increased substrate interface energy and preferential (111) facet growth highlights a robust interface energy-driven crystallization mechanism. The results indicate a ~~novel~~ strategy for facet-selective synthesis, particularly enabling precise (111)-oriented crystal engineering through substrate surface energy modulation. Such insights could advance applications in optoelectronics requiring controlled crystal morphologies.

To demonstrate the universality of the proposed strategy, various hydrophobic substrates with high-surface-energy (e.g., PDMS, hydrophobic glass, and PET) are employed for the microdroplet-based solid-liquid interface synthesis. The optical microscope images demonstrating crystal growth on these substrates and their corresponding XRD patterns are provided in Supplementary Fig. 7 and Figs. 3a–c, respectively. It's evident that the batch preparation of (111)-oriented CABB PSCs can be achieved on these three substrates. And the XRD results confirm that all three substrates exclusively exhibit diffraction signals from the {111} facet family, with no detectable {100} or {110} signals. In addition to CABB PSCs, we have also performed parallel experiments on $CsPbBr_3$ single crystals because of their structural similarity (*P*m-3m for the high-temperature phase of $CsPbBr_3$ and *F*m-3m for CABB). As a result (Supplementary Fig. 8), different from traditional rectangular prism habit, the as-grown $CsPbBr_3$ crystals exhibit a distinct rhombohedral shape and also have a preferred orientation. Correspondingly, the XRD spectrum reveals the presence of closely-arranged {210} signals, thereby confirming the effective

applicability of the interface synthesis method. The underlying mechanism of controlling the facets lies in the interfacial solute aggregation effect dominated by the interface energy. In this case, the nucleation barrier of (111) facets can be selectively reduced because of the high interface energy of the hydrophobic substrates (Fig. 3d). According to Young's equation, the equilibrium state of the interaction between solid and liquid on the substrates can be written as[31]:

$$\gamma_{sl} = \gamma_{sv} - \gamma_{vl}\cos\theta \quad (1)$$

where θ represents contact angle, γ_{sv}, γ_{vl}, γ_{sl} are the interfacial energy of solid-vapor, vapor-liquid, solid-liquid interfaces, respectively. As illustrated in Fig. 3e, hydrophobic substrates with high γ_{sv} repels water molecules, resulting in a significant increase in the local concentration of solutes at the solid-liquid interface and creating a localized solute-enriched region at the solid-liquid interface. This micro-environment preferentially stabilizes the (111) facets because of the close-packed characteristic with the lowest surface energy. Additionally, continuous depletion of solute in the interface layer generates a concentration gradient of monomers, further driving the solute in solution to diffuse to the solid-liquid interface (Supplementary Fig. 9). This interface layer is formed by the dissolution of precursors and is affected by the concentration gradient of monomers, whereby near-stoichiometry is maintained by dissolving clusters to replenish cation-deficient zones[26]. On the contrary, hydrophilic substrates with low γ_{sv} allow discrete solute spreading, leading to heterogeneous nucleation across multiple facets. Morphologically, the CABB crystals with (111)-preferred orientation adopt a octahedral shape (Fig. 3f), with triangle and hexagonal terminations reflecting their close-packed symmetry (Fig. 3g and Supplementary Fig. 10). The octahedral morphology of CABB PSCs stems from the intrinsic face-centered cubic (FCC) lattice symmetry (space group *F*m-3m) and the thermodynamic imperative for

surface energy minimization. As the central top triangle and bottom hexagonal (111) surface grow laterally, the six sides adopt the shape of a truncated triangle, ultimately achieving octahedral morphology. Calculated from the EDS analysis of the elemental content (Supplementary Fig. 11), the stoichiometric ratios of Cs:Ag:Bi:Br are found to be 2.2:0.9:1.0:6.9 and 2.2:0.8:1.0:7.1, which basically agree with the theoretical ratio of 2:1:1:6. The deviation from the standard value stems from the Br-rich growth environment and the CABB crystal surfaces are energetically favored to be terminated by the more stable Br surface layers. In addition, the high quality of the (111) facets are revealed by AFM images (Supplementary Fig. 12), exhibiting a surface roughness of only 0.3 nm. These results unambiguously demonstrate the universal effectiveness of high-interface-energy substrates in achieving (111)-oriented growth. Essentially, this method is the spatial modulation of nucleation dynamic by interface engineering. The preferred control of crystal orientation is achieved by constructing local high-throughput solute supply condition.

As is well-known that ionic migration and lattice distortion are critical factors contributing to the phase decomposition and the degradation of device performance[32,33]. Conducting in-depth investigation on ion migration kinetics and the lattice strain release holds great significance for improving the stability of perovskite materials and the performance of devices. The ionic nature of CABB is revealed by the transient current discharge test (Fig. 4a). Upon sudden removal of external bias, the relaxation process exhibits a negative recoil current, which is composed of the superposition of electronic current (I_e) and ion diffusion current (I_{ion}) driven by concentration gradients. The observed negative current spike is the instantaneous sum of these two components ($I_{total} = I_e + I_{ion}$), I_e and I_{ion} jointly superimpose into the largest negative current instantly after the bias was off. As the discharge progresses, the ion migration gradually

equilibrates the internal charge distribution, reducing the driving force for ion migration and leading a decay in current. To determine and compare the ion migration barriers of four types ions in CABB, first-principles calculation is applied. As depicted in Fig. 4b, the calculation reveals that Br^- and Ag^+ are easier to migrate, with energy barriers of ~0.15 eV and ~0.75 eV, respectively. The calculated energy band structure of CABB is shown in Fig. 4c, indicating an indirect bandgap of ~2.13 eV. Given that in hybrid halide PSCs, the ion migration barriers are highly dependent on the crystal orientation and migration pathways. Thus, for Br^- and Ag^+, we select the shortest migration path (Fig. 4g) and further calculate the Br^-/Ag^+ ion migration energy (IME) and vacancy formation energy (VFE) in different facets. The calculated results demonstrate that Br^- exhibits the lowest migration barrier among all ionic species in CABB system (Fig. 4e). Therefore, Br^- migration is kinetically favored as the primary degradation pathway, which is consistent with established literature indicating that halogen migration represents the dominant failure mechanism in perovskite materials. The (111) facet possesses the highest Ag^+ IME (3.43 eV) and largest V_{Br}^+/V_{Ag}^- VFE (1.45/2.42 eV), indicating that the ion migration phenomenon can be significantly suppressed at the (111) facet.

Although the mixed cations of Ag^+ and Bi^{3+} demonstrate a positive effect on suppressing non-radiative recombination, the consequent tensile strain induced by the disordered arrangement of $[AgBr_6]^{5-}$ and $[BiBr_6]^{3-}$ octahedron easily leads to non-uniform stress[34,35]. To release internal lattice stress and induce $[AgBr_6]^{5-}/[BiBr_6]^{3-}$ ordering, thermal annealing is adopted. Due to the electron-beam sensitivity of CABB perovskites, it remains challenging to directly observe lattice strain relief and defect reduction by transmission electron microscopy (Supplementary Fig. 13). Indirectly, as evidenced by XRD comparisons (Fig. 4d), thermal treatment at 200 ℃ for 1 hour effectively mitigates lattice distortion. After annealing,

the diffraction peaks shift toward higher angles (lattice contraction), with reduced FWHM from 0.05° to 0.03° at the high-angle peak position, demonstrating diminished strain and improved crystallinity. To exclude the possibility of composition change, we conducted post-annealing elemental content verification by EDS analysis (Supplementary Fig. 14 and Supplementary Table 3). The compared EDS analysis results confirm the retention of stoichiometry after annealing, thereby indicating that the XRD peak shift originates from strain relaxation rather than composition change. Fig. 4f illustrates the mechanism of the lattice strain release process. Critically, the optimal annealing protocol (200 ℃ for 1 hour) balances kinetic reorganization and thermodynamic stability. Thermal energy provides critical activation for defect migration via synergistic pathways. During the annealing process, the increase of temperature intensifies the atomic vibration. The enhanced atomic vibration amplitude enables Br^- to overcome the energy barrier and occupy the distorted lattice sites, directly reducing trap densities. Besides, the post-annealing process allows the $[AgBr_6]^{5-}$/$[BiBr_6]^{3-}$ octahedra to gradually and orderly rearrange, transforming the high-entropy states inside the crystal into a low-entropy state. Upon being provided with enough activation energy at high temperature, Bi^{3+} and Ag^+ could move back into their own octahedral sites and reorganize in a more ordered manner. The movements of ions also help in redistributing residual strain within the crystal lattice, leading to a more stable and durable structure[36]. After cooling, Ag^+/Bi^{3+} ions no longer have the thermal energy required for further ion mobility, thus allowing the previously rearranged ordered structure to be retained. By reorganizing the lattice via atomic rearrangement and redistributing residual strain, the overall structure becomes more uniform. Besides, the annealing-induced strain release process could further stabilize the crystal lattice, eliminate defects and reduce activation sites for ion diffusion.

Further, the optical, thermal and electronic properties of CABB PSCs are systematically surveyed, with focus on crystallographic orientation effects and post-annealing optimization. The UV-vis absorption spectrum of CABB (Fig. 5a) exhibits the features of an indirect bandgap semiconductor, characterized by a shallow absorption region beginning at 700 nm followed by a sharp increase in absorption near 600 nm. The Tauc-plot fitting of data is shown in the inset. The linear regions correspond to the phonon-assisted processes, where transitions at 1.82 and 2.15 eV are associated with phonon absorption and emission, respectively. The indirect bandgap of CABB is estimated as 1.99 eV with an assisting phonon energy of 0.17 eV, which is basically consistent with our previously calculated energy band diagram. The deviation of bandgap value stems from the strong spin-orbit coupling effects between Ag and Bi, which can over-correct the initial GGA underestimation and result in a final bandgap that is slightly larger than the experimental value. Confocal photoluminescence (PL) spectroscopy (Fig. 5b) demonstrates orientation-dependent emission behavior. All facets (100), (110) and (111) exhibit a PL peak at 650 nm, but the intensity follows the order (100)＞(110)＞(111). The weakest PL of (111) facet indicates suppressed radiative recombination, attributed to its dense atomic packing and minimized defect density. As shown in Fig. 5c, thermogravimetric analysis (TGA) reveals exceptional thermal stability of the as-synthesized CABB PSCs, with sample maintaining structural integrity up to 460 ℃. In comparison, organic-inorganic hybrid perovskites such as $MAPbI_3$ decomposes only at ~250 ℃[37]. The high decomposition temperature stems from robust ionic boding between Cs^+ and $[AgBr_6]^{5-}$-$[BiBr_6]^{3-}$ framework, as well as the absence of volatile organic components. After thermal annealing, the PL peak of (111) facet obviously blueshifts from 650 nm to 600 nm, and the FWHM decreases from 166 nm to 113 nm (Fig. 5d). This signifies defect healing and strain relaxation, as lattice reconstruction during annealing eliminates mid-gap trap states

responsible for sub-bandgap emission. Fundamentally, the ~50 nm blueshift in PL spectra stems from synergistic structural and electronic reorganization induced by thermal annealing, which enhances the near-band-edge emission while blueshifting the PL peak. Before annealing, compressive lattice strain decreases bond angles (Ag/Bi−Br), narrowing the bandgap via atomic orbital overlap and hybridization. After annealing, strain relaxation enlarges angles (Supplementary Fig. 15), thus widening the bandgap by ~0.16 eV (blueshift Δλ ~50 nm) by reducing the orbital overlap. To avoid accidental factors, multi-point repeated PL tests on the (111) facet are performed (Supplementary Fig. 16). The PL peak positions are all around 600 nm, indicating the uniformity of the surface and the improvement effect of annealing treatment. The trap density reduction is also observed in the current-voltage curves of pristine and annealed CABB PSCs (Supplementary Fig. 17). After annealing, the trap density is calculated to decrease from 4.58×10^9 cm^{-3} to 1.45×10^9 cm^{-3}. Time-resolved photoluminescence (TRPL) measurements of (111) facet (Fig. 5e) quantify carrier lifetime improvements after annealing. The formula for calculating the average carrier lifetime can be written as follows:

$$\tau_{avg} = \frac{A_1\tau_1^{\ 2} + A_2\tau_2^{\ 2}}{A_1\tau_1 + A_2\tau_2} \quad (2)$$

where τ_1 is short lifetime, τ_2 is long lifetime, A_1 and A_2 are the corresponding fractional contributions. It can be seen that the average carrier lifetime increases from 1.5 ns (as-grown) to 6.2 ns (annealed), reflecting reduced non-radiative recombination via defect passivation. The prolonged carrier lifetime is beneficial for reducing non-radiative losses improving the photocurrent generation efficiency. In term of electronic properties, the resistivity of (111) facet rises from 3.49×10^{10} Ω cm to 3.85×10^{11} Ω cm (Fig. 5f). The increased resistivity is attributed to diminished ionic pathways and suppressed defect-mediated conduction. This higher resistivity leads to lower dark current, which is beneficial for photodetection.

These results underscore the role of annealing in simultaneously optimizing photo-generated carriers and electronic transport properties, establishing foundations for high-gain photodetectors.

To investigate the orientation-dependent optoelectronic properties of CABB PSCs, metal-semiconductor-metal (MSM) two-terminal devices are fabricated on (100)/(110)/(111) facets using a mesh-style metal mask (Supplementary Fig. 18) and vacuum-deposited gold electrodes (40 nm thickness, ~25 μm channel width, Supplementary Fig. 19). The MSM architecture provides an ideal platform to evaluate facet-dependent optoelectronic performance due to its intrinsic carrier transport characteristics. In this structure, photo-generated carriers are rapidly separated under an external electric field and collected by adjacent metal electrodes, minimizing bulk recombination losses[38]. Based on the as-synthesized facets, three kinds of photodetectors are constructed and compared. Specifically, current-voltage (*I–V*) measurements (Fig. 5g) reveal an obvious orientation dependence, with dark current values decreasing in the order (100) ($>10^{-11}$ A)＞(110) (~8 pA)＞(111) (~3 pA) at 3 V bias. The low dark current (pA-level) of (111) facet stems from its intrinsic high ion migration activation energy and suppressed trap-assisted tunneling, thus reducing carrier scattering and non-radiative recombination. Fig. 5h demonstrates the statistical datasets of photo/dark currents of the three kinds of crystal facets, highlighting the best on/off performance of the (111) facets. Under the same 500 nm light illumination with an intensity of 2.8 mW cm^{-2}, photocurrent follows the trend: (111)(~1.1 nA)＞(110)(~0.9 nA)＞(100) (~0.2 nA), highlighting the prominent photoresponse ability of (111) facets. The (111)-orientated device exhibits excellent photoresponse capabilities to visible light, with the optimal response wavelength being approximately 500 nm (Supplementary Fig. 20). An on/off ratio of ~350 at 500 nm and a peak responsivity of 332 mA W^{-1} at 520 nm (Fig. 5i) are achieved by the (111) facet-based device, both of which are superior to (100) and

(110) facets. And it's worth noting that the discrepancy between the optimal response wavelength (520 nm) and the PL peak (600-650 nm) stems from the indirect bandgap characteristic of CABB materials. Because the direct transition of valence band electrons to the conduction band requires higher energy than the indirect transition, the spatial separation of excitation and recombination pathways causes an obvious red-shift in PL emission (600-650 nm) compared with the efficient generation of carriers (520 nm). Moreover, the response speed for (100), (110), and (111)-oriented photodetectors under identical testing conditions (520 nm illumination, 3 V bias) are compared in Supplementary Table 4. Specifically, the (111)-oriented devices exhibit optimal steady-state response speed (τ_{rise}/τ_{decay} = 0.65/1.23 s), faster than (100)/(110) devices due to anisotropic carrier transport behaviors. The best optoelectronic properties of (111) facets are attributed to the anisotropic carrier mobility favoring efficient charge extraction along the [111] direction, governed by crystallographic symmetry and defect density. Based on previously reported work[39], we reasonably speculate that the close-packed Ag-Bi-Br arrangement within the (111) facets lead to a decreased inter-atomic distance, promoting electron orbital overlap and thus enhancing the carrier mobility. Stability assessments (Supplementary Fig. 21) further underscored the (111) facet's robustness: unencapsulated devices retained >90% of initial photoresponse capability after 30 days in ambient air environment (25°C, 60% RH), vastly outperforming lead-based organic-inorganic hybrid perovskites. This environmental resilience also originates from the dense atomic packing of the (111) facet, which impedes moisture infiltration and ion diffusion. The synergy between the (111) facet's reduced dark current, boosted photocurrent and stable interfacial energetics establishes CABB as a prospective candidate for durable perovskite-based optoelectronics. This discovery of the anisotropic orientation-dependent optoelectronic properties of CABB PSCs provides a design strategy in crystallographic

optimization for developing high-performance optoelectronic devices.

In summary, we successfully synthesized high-quality CABB PSCs with (111)-preferred orientation at the solid-liquid interface and demonstrated the strategy universality of growing specific crystallographic facets using substrates with high interface energy. Both theoretical and experimental results validate the advantages of (111)-orientation facets with higher ionic migrate energy and lower defect density, which results in excellent stability. Besides, thermal annealing is adopted to further improve the crystal quality of the (111)-orientation CABB PSCs. After annealing, the XRD peaks shift rightward with narrowed FWHM (from 0.05° to 0.03°), indicating reduced lattice distortion. Concurrently, the PL emission blueshifts from 650 nm to 600 nm, accompanied by a decreased FWHM from 166 nm to 113 nm. And the carrier lifetime revealed by TRPL increases from 1.5 ns to 6.2 ns. Additionally, the resistivity of (111) facet rises from 3.49 $\times 10^{10}$ Ω cm to 3.85 $\times 10^{11}$ Ω cm after annealing. These results validate thermal annealing as a beneficial strategy that provides energy to induce the release of internal lattice stress and achieve the orderly arrangement of $[AgBr_6]^{5-}/[BiBr_6]^{3-}$. Moreover, the potential application of CABB facets in optoelectronic devices is explored. Photodetectors based on the (111) facets exhibit the best performance, featuring suppressed dark currents on the order of 10^{-12} A, enhanced photocurrents exceeding 10^{-9} A, and a peak responsivity as high as 332 mA W^{-1}. The research on the anisotropy of lead-free CABB PSCs in this work reveals the orientation-dependent physical properties of the crystal facets, providing crucial theoretical basis and material design guidance for the development of green energy technologies.

Methods

Single crystal growth. The CABB PSCs were grown using solution evaporation crystallization method.

This optimized method can improve the dimensional integrity of PSCs and control the defect density by modulating the solution concentration, solvent evaporation rate and annealing temperature. The precursor solution was prepared by dissolving CsBr, AgBr and $BiBr_3$ (2:1:1 molar ratio) in aqueous hydroiodic acid (HBr, 48.0 wt% in H_2O, 99.99%), with a concentration of 0.03 M. After magnetic stirring to fully dissolved, the solution was filtered through a 0.22 μm polytetrafluoroethylene (PTFE) filter before use. Using a pipette, 5-10 μL precursor droplet was dropped onto a clean and hydrophobic substrate, which was then placed on a hot plate of 60 °C in an open ambient environment. Driven by the solution supersaturation and high interface energy of the substrate, CABB PSCs with (111) facets nucleated at the solid–liquid interface and subsequently grew until the solvent was completely evaporated. The hydrophobic treatment of the Si/SiO_2 substrates was carried out using an immersion method. Specifically, the Si/SiO_2 substrates were immersed in a mixture of hexane and OTS (octadecyltrichlorosilane) at a volume ratio of 500:1 for 2 hours. Subsequently, the substrates were thoroughly cleaned by sequential ultrasonication in hexane, chloroform, and isopropanol to obtain the hydrophobic Si/SiO_2 substrates. Typically, the initiating nucleation occurred within 2 minutes and the entire crystal growth required maintaining the microdroplet for over 20 min. Finally, the obtained PSCs were annealed at 200 ℃ for 1 hour to release internal stress and minimize lattice distortion. The growth processes were all conducted in an open ambient environment.

Theoretical calculations. All calculations were performed based on the density functional theory (DFT). The PBE (Perdew-Burke-Ernzerhof)-GGA (generalized gradient approximation) functional and PAW (projected augmented wave) method are used with the energy cutoff of 520 eV. The geometry optimizations used stringent convergence thresholds (energy change per atom ≤ 1×10^{-6} eV, max force ≤

0.01 eV $Å^{-1}$, max stress ≤ 0.02 GPa, max displacement ≤ $5×10^{-4}$ Å). SCF cycles were converged to an electronic energy tolerance ≤ $1×10^{-6}$ eV $atom^{-1}$. Brillouin-zone sampling employed Monkhorst–Pack meshes that we converged until the total-energy change was < 1 meV $atom^{-1}$. The k-point mesh was set to 1×1×1. To capture the spin-orbit effects in Bi, all key electronic-structure results were recomputed with non-collinear magnetism and spin–orbit coupling enabled. Compared with the methods presented in the literature, similar computational requirements for calculation accuracy have been adopted.

General characterizations. XRD patterns were collected by an X-ray diffractometer (Bruker D8 Advance, Cu Kα, λ = 1.5406 Å). SEM images and EDS mappings were acquired by a field scanning electron microscope (Zeiss Sigma 300). XPS spectra were obtained by an X-ray photoelectron spectrometer (Thermo Scientific ESCALAB 250XI). Optical photographs were captured by an optical microscope (Olympus, BX51M). UV-vis absorption spectrum was acquired by a spectrometer (Hitachi U-3900H). PL results were performed at a muti-functional confocal Raman microscope equipped with 532 nm laser excitation (Renishaw inVia-Qontor). TRPL spectrum was obtained by a transient fluorescence spectrometer using 450 nm laser excitation (HORIBA). TGA experiment was conducted by a thermal gravimetric analyzer (TA Q500). AFM results were performed by a scanning probe microscope (Bruker Dimension Edge). Thickness profiles were determined by a step profiler (KLA-Tencor).

Device fabrication and test. The photodetectors adopted the common MSM structure. Symmetric Au electrodes were thermal evaporated in vacuum onto different crystallographic facets (100), (110) and (111) using metal physical mask with a hollow design (Supplementary Fig. 18). The mesh-style mask partially blocks the deposition of metal, creating gaps between adjacent electrodes which function as micro-channels. As a result, the channel spacing was ~ 25 μm, and the Au thickness was approximately 40 nm.

The electrical and optoelectronic performance of the as-fabricated devices were measured by a semiconductor characterization system (Keithley 4200-SCS) connected to a vacuum probe station (Lake Shore). A 75 W Xe lamp equipped with a monochromator was used as a light source. All the tests were performed under ambient conditions at room temperature.

Data Availability

All data supporting this work are available within the paper and Supplementary Information. Any additional data are available from the corresponding author on ~~reasonable~~ request. Source data are provided with this paper.

References

1 Zhao, L. et al. High-yield growth of $FACsPbBr_3$ single crystals with low defect density from mixed solvents for gamma-ray spectroscopy. *Nat. Photon.* **17**, 315-323 (2023).

2 Chen, G. Y. et al. Nucleation-mediated growth of chiral 3D organic-inorganic perovskite single crystals. *Nat. Chem.* **15**, 1581-1590 (2023).

3 Cao, F. et al. Lead-free single crystal metal halide perovskite detectors. *Mater. Sci. Eng. R* **164**, 100991 (2025).

4 Zhang, Y. X. et al. Nucleation-controlled growth of superior lead-free perovskite $Cs_3Bi_2I_9$ single-crystals for high-performance X-ray detection. *Nat. Commun.* **11**, 2304 (2020).

5 Connor, B. A., Leppert, L., Smith, M. D., Neaton, J. B. & Karunadasa, H. I. Layered halide double perovskites: dimensional reduction of $Cs_2AgBiBr_6$. *J. Am. Chem. Soc.* **140**, 5235-5240 (2018).

6 Yu, W. J. et al. Breaking the bottleneck of lead-free perovskite solar cells through dimensionality modulation. *Chem. Soc. Rev.* **53**, 1769-1788 (2024).

7 Zhang, X. et al. Self-assembly of 2D hybrid double perovskites on 3D $Cs_2AgBiBr_6$ crystals towards ultrasensitive detection of weak polarized light. *Angew. Chem. Int. Ed.* **61**, e202205939 (2022).

8 Pan, W. C. et al. $Cs_2AgBiBr_6$ single-crystal X-ray detectors with a low detection limit. *Nat. Photon.* **11**, 726-732 (2017).

9 Deng, M., Li, Z. Q., Liu, S. Y., Fang, X. S. & Wu, L. M. Wafer-scale integration of two-dimensional perovskite oxides towards motion recognition. *Nat. Commun.* **15**, 8789 (2024).

10 Zhang, X., Li, Z., Hong, E., Yan, T. & Fang, X. Effective dual cation release in quasi-2D perovskites for ultrafast UV light-powered imaging. *Adv. Mater.* **37**, 2412014 (2024).

11 Hu, Y. et al. High-purity photoactive α-phase for flexible perovskite photodetectors with modified electron transport layer. *Adv. Funct. Mater.* **35**, 2412015 (2025).

12 Hong, E., Li, Z., Zhang, X., Fan, X. & Fang, X. Deterministic fabrication and quantum-well modulation of phase-pure 2D perovskite heterostructures for encrypted light communication. *Adv. Mater.* **36**, 2400365 (2024).

13 Wei, Y. et al. Recent progress of bismuth effect on all-inorganic lead-free metal halide derivatives: crystals structure, luminescence properties, and applications. *Adv. Funct. Mater.* **33**, 2205829 (2023).

14 Feng, J. G., Qiu, Y. C., Jiang, L. & Wu, Y. C. Long-range-ordered assembly of micro-/nanostructures at superwetting interfaces. *Adv. Mater.* **34**, 2106857 (2022).

15 Ricciardulli, A. G., Yang, S., Smet, J. H. & Saliba, M. Emerging perovskite monolayers. *Nat. Mater.* **20**, 1325-1336 (2021).

16 Pan, L. F. et al. High carrier mobility along the [111] orientation in Cu_2O photoelectrodes. *Nature* **628**, 765-770 (2024).

17 Dong, S. H. et al. All-inorganic perovskite single-crystal photoelectric anisotropy. *Adv. Mater.* **34**, 2204342 (2022).

18 Wang, Y. et al. Facet engineering and pore design boost dynamic Fe exchange in oxygen evolution catalysis to break the activity-stability trade-off. *J. Am. Chem. Soc.* **145**, 20261-20272 (2023).

19 Liu, Z. et al. All-perovskite tandem solar cells achieving >29% efficiency with improved (100) orientation in wide-bandgap perovskites. *Nat. Mater.* **24**, 252-259 (2025).

20 Hsiao, Y. C. et al. A library of seed@high-entropy-alloy core-shell nanocrystals with controlled facets for catalysis. *Adv. Mater.* **37**, 2411464 (2025).

21 Xia, P. et al. Improved facet and edge passivation in near-infrared III-V colloidal quantum dot photodetectors. *Adv. Mater.* **37**, 2419020 (2025).

22 Yao, Y. X. et al. Oriented wide-bandgap perovskites for monolithic silicon-based tandems with over

1000 hours operational stability. *Nat. Commun.* **16**, 40 (2025).

23 Ma, C. Q. et al. Unveiling facet-dependent degradation and facet engineering for stable perovskite solar cells. *Science* **379**, 173-178 (2023).

24 Xia, M. et al. Kinetic Wulff-shaped heteroepitaxy of phase-pure 2D perovskite heterostructures with deterministic slab thickness. *Nat. Synth.* **4**, 380-390 (2025).

25 Read, C. G., Steinmiller, E. M. P. & Choi, K. S. Atomic pane-selective deposition of gold nanoparticles on metal oxide crystals exploiting preferential adsorption of additives. *J. Am. Chem. Soc.* **131**, 12040-12041 (2009).

26 Shi, Z. et al. Self-regulated facet stability during solution growth of perovskite crystals. *Nat. Synth.* **4**, 1088-1094 (2025).

27 Wang, J. W. et al. Facet-engineered growth of non-layered 2D manganese chalcogenides. *Adv. Powder Mater.* **3**, 100164 (2024).

28 Chen, C. S. et al. Fluid chemistry of metal halide perovskites. *Angew. Chem. Int. Ed.* **64**, e202503593 (2025).

29 Hong, E., Li, Z., Yan, T. & Fang, X. Surface-tension-dominant crystallization of 2D perovskite single crystals for vertically oriented hetero-/homo-structure photodetectors. *Nano Lett.* **22**, 8662-8669 (2022).

30 Zhang, Y. et al. Crystal facet engineering on $SrTiO_3$ enhances photocatalytic overall water splitting. *J. Am. Chem. Soc.* **146**, 6618-6627 (2024).

31 Prydatko, A. V., Belyaeva, L. A., Jiang, L., Lima, L. M. C. & Schneider, G. F. Contact angle measurement of free-standing square-millimeter single-layer graphene. *Nat. Commun.* **9**, 4185 (2018).

32 Qu, S. J. et al. Revealing and inhibiting the facet-related ion migration for efficient and stable perovskite solar cells. *Angew. Chem. Int. Ed.* **64**, e202415949 (2024).

33 Akriti et al. Layer-by-layer anionic diffusion in two-dimensional halide perovskite vertical heterostructures. *Nat. Nanotechnol.* **16**, 584-591 (2021).

34 Jiang, J. et al. Synergistic strain engineering of perovskite single crystals for highly stable and sensitive X-ray detectors with low-bias imaging and monitoring. *Nat. Photon.* **16**, 575-581 (2022).

35 Yang, X. Y. et al. In-line tempering eliminates the domain boundary in perovskite single crystals for

high-energy resolution ionizing radiation detectors. *Sci. Adv.* **10**, eadq6866 (2024).

36 Shen, Y. X. et al. Strain regulation retards natural operation decay of perovskite solar cells. *Nature* **635**, 882-889 (2024).

37 Nagabhushana, G. P., Shivaramaiah, R. & Navrotsky, A. Direct calorimetric verification of thermodynamic instability of lead halide hybrid perovskites. *Proc. Natl. Acad. Sci. U.S.A.* **113**, 7717-7721 (2016).

38 Wang, F., Zhang, T., Xie, R. Z., Wang, Z. & Hu, W. D. How to characterize figures of merit of two-dimensional photodetectors. *Nat. Commun.* **14**, 2224 (2023).

39 Wang, Z. Y., Wang, M. C., Heine, T. & Feng, X. L. Electronic and quantum properties of organic two-dimensional crystals. *Nat. Rev. Mater.* **10**, 147-166 (2025).

Acknowledgements

This work was supported by the National Natural Science Foundation of China (Nos. 52425308 (X.F.), 524B2017 (E.H.), 62374035 (X.F.) and 92263106 (X.F.)).

Author contributions

Z.L., L.W. and X.F. conceived the idea. Z.L. and E.H. designed the experiments. E.H. carried out the material synthesis and related characteristics. M.D. provided helpful suggestions about crystal growth and TRPL measurements. E.H., Z.L. and X.F. wrote and revised the manuscript. All authors reviewed and approved the paper.

Competing interests

The remaining authors declare no competing financial interests.

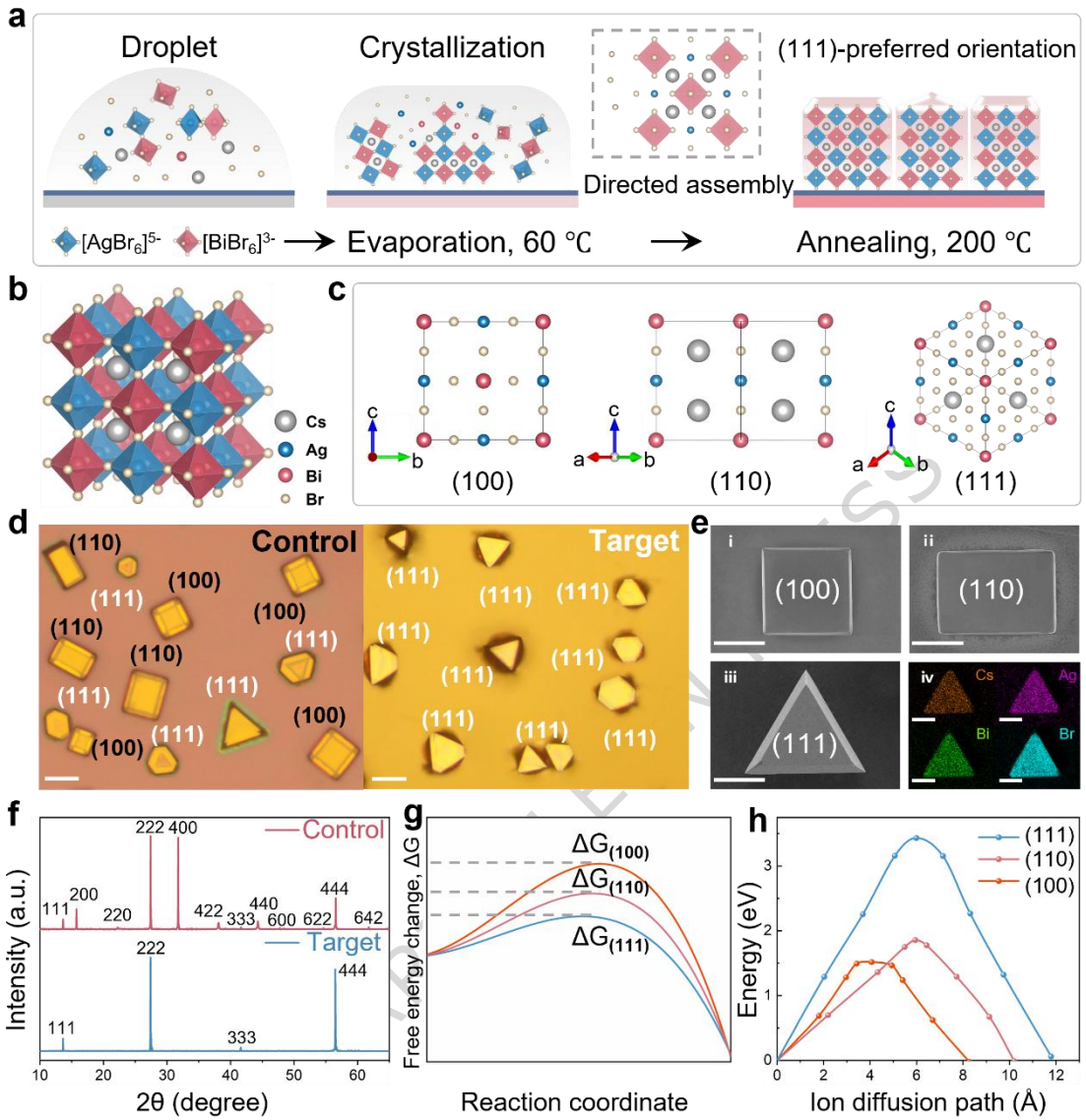

Fig. 1 | Solid-liquid interface synthesis of CABB single crystals. a, Schematic illustrations of the crystallization and annealing processes. **b,** Crystal structure of CABB. **c,** Schematic diagrams of the (100) (110) and (111) facets, respectively. **d,** Optical images of the control (Si/SiO_2 substrate) and target (PDMS substrate) groups, respectively. Scale bar: 50 μm. **e,** SEM images of (100)/(110)/(111) facets (i–iii) and corresponding elemental mappings of (111) facet (iv). Scale bar: 50 μm. **f,** XRD results of the control and target groups (Miller indices of the facets are labeled). **g,** Illustration of the activation barriers of different facets. **h,** DFT results for the Ag^+ ion migration energies in (100)/(110)/(111) facets.

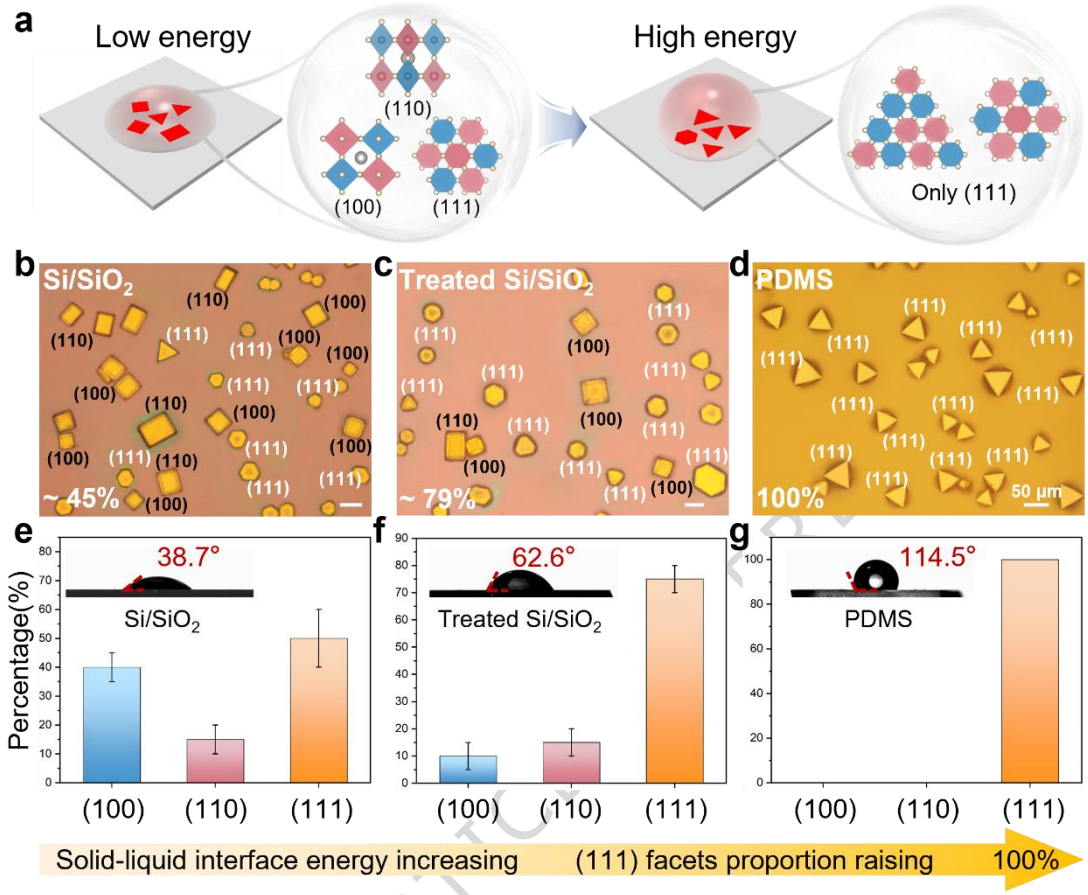

Fig. 2 | The role of substrate interface energy in regulating facet proportions of CABB crystals. a. Schematic illustrations of solid-liquid interface growth of CABB crystals. **b-d,** Optical images of the crystal growth situations on pristine Si/SiO_2, treated Si/SiO_2 and PDMS substrates, respectively. **e-g,** Statistical data on the proportion of different facets on a wide field of view. The error bars represent the standard deviation and are calculated based on the variation in the percentages, n = 3. Inset: contact-angle images of droplets on each substrate.

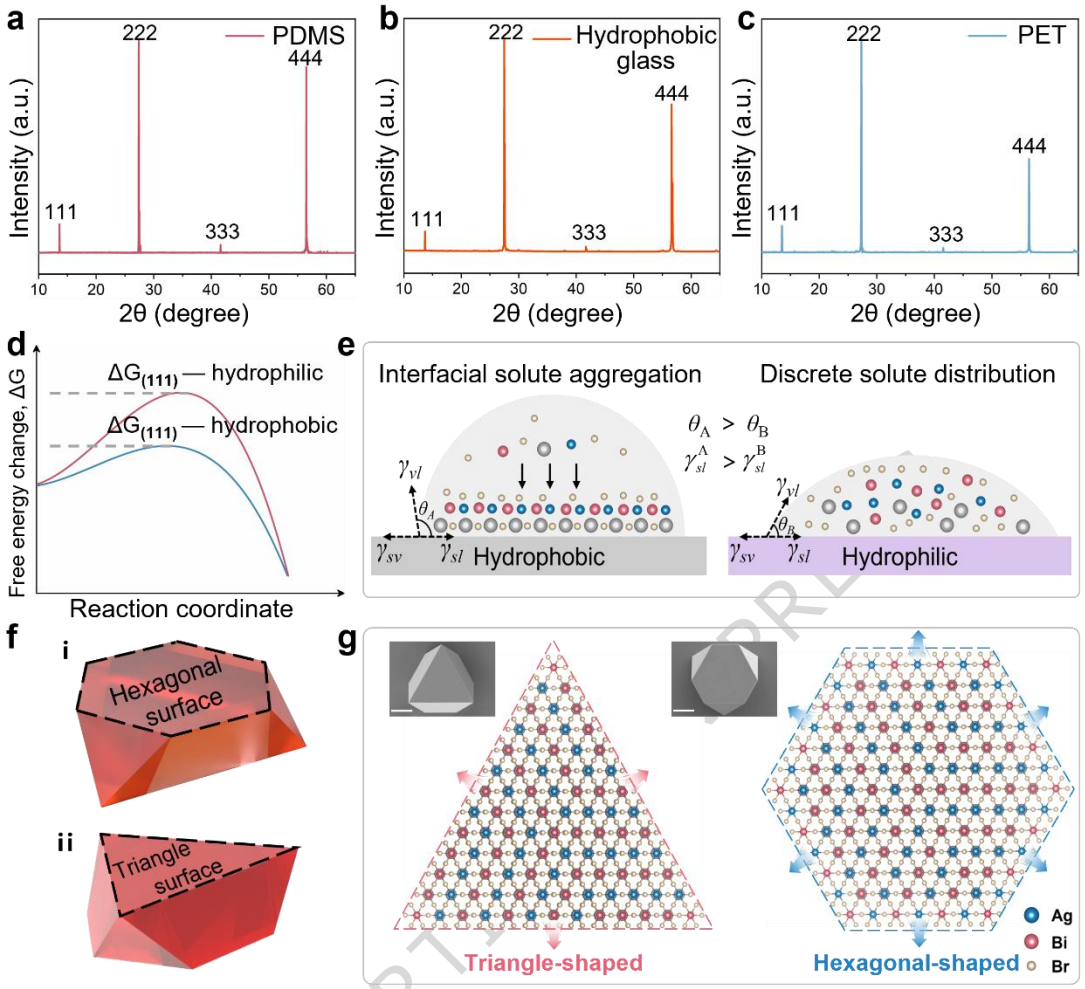

Fig. 3 | Universality demonstrations and mechanism analysis of the (111)-preferred orientation. a–c, Corresponding XRD results of as-grown CABB samples on different substrates. **d,** Illustration of the activation barriers in different substrates. **e,** Schematics of interface nucleation of crystals from microdroplets on hydrophobic and hydrophilic substrates. γ_{sv}, γ_{vl}, γ_{sl} are the interfacial energy of solid-vapor, vapor-liquid, solid-liquid interfaces, respectively. **f,** Crystal models of CABB with (111) orientation and octahedral shape. **g,** Atomic illustrations of the triangle-shaped and hexagonal-shaped (111) facets. Inset: SEM images of CABB single crystals. Scale bar: 50 μm.

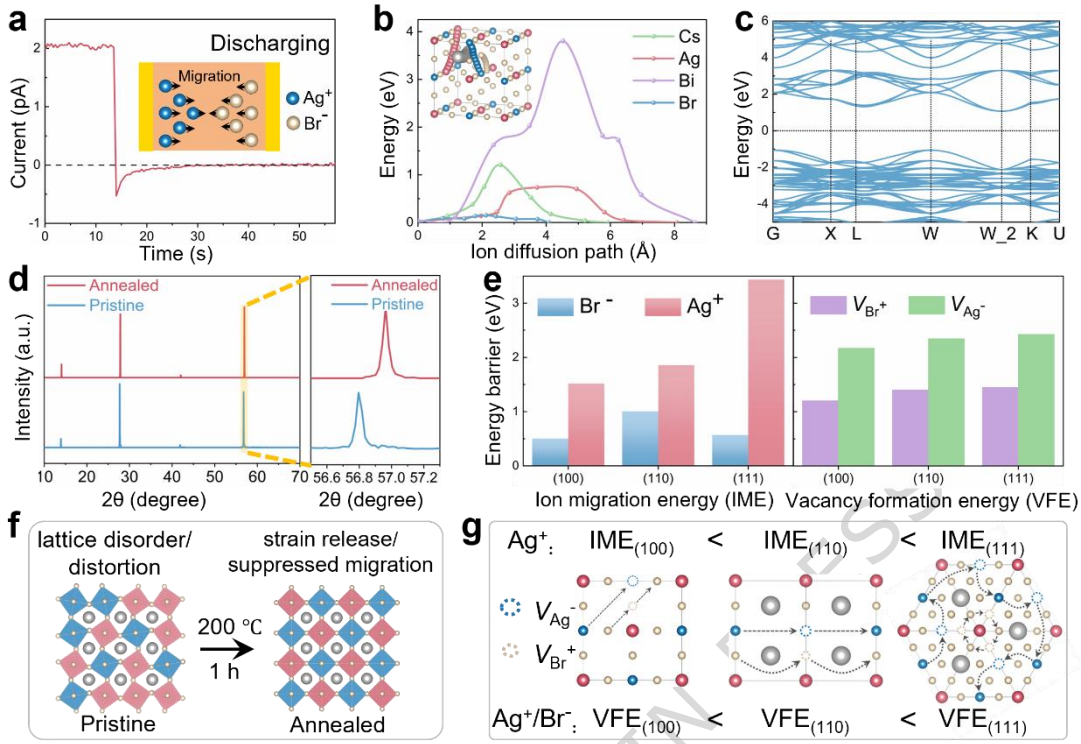

Fig. 4 | Ionic migration characteristic investigation and lattice strain release of CABB PSCs. a, Transient current discharge curve of the CABB–based device. Inset: Schematic illustration of the discharging process during the ionic migration measurement upon turning off the external bias. **b,** Calculated ion migration energy profile along the diffusion path for the possible ion vacancies in CABB, indicating the easy migration characteristic of Ag^+ and Br^-. Inset: Schematic diagram of ion migration paths inside the crystal structure. **c,** Calculated band structure of CABB, indicating the indirect bandgap characteristic. **d,** XRD spectra of CABB PSCs before and after annealed. **e,** Calculated IME and VFE of Ag^+ and Br^- in different facets of CABB. **f,** Schematic of the local lattice strain inside crystals, which can be relaxed by annealing. **g,** Schematic illustrations of the ion migration pathways for Ag^+ and Br^- in (100), (110) and (111) facets.

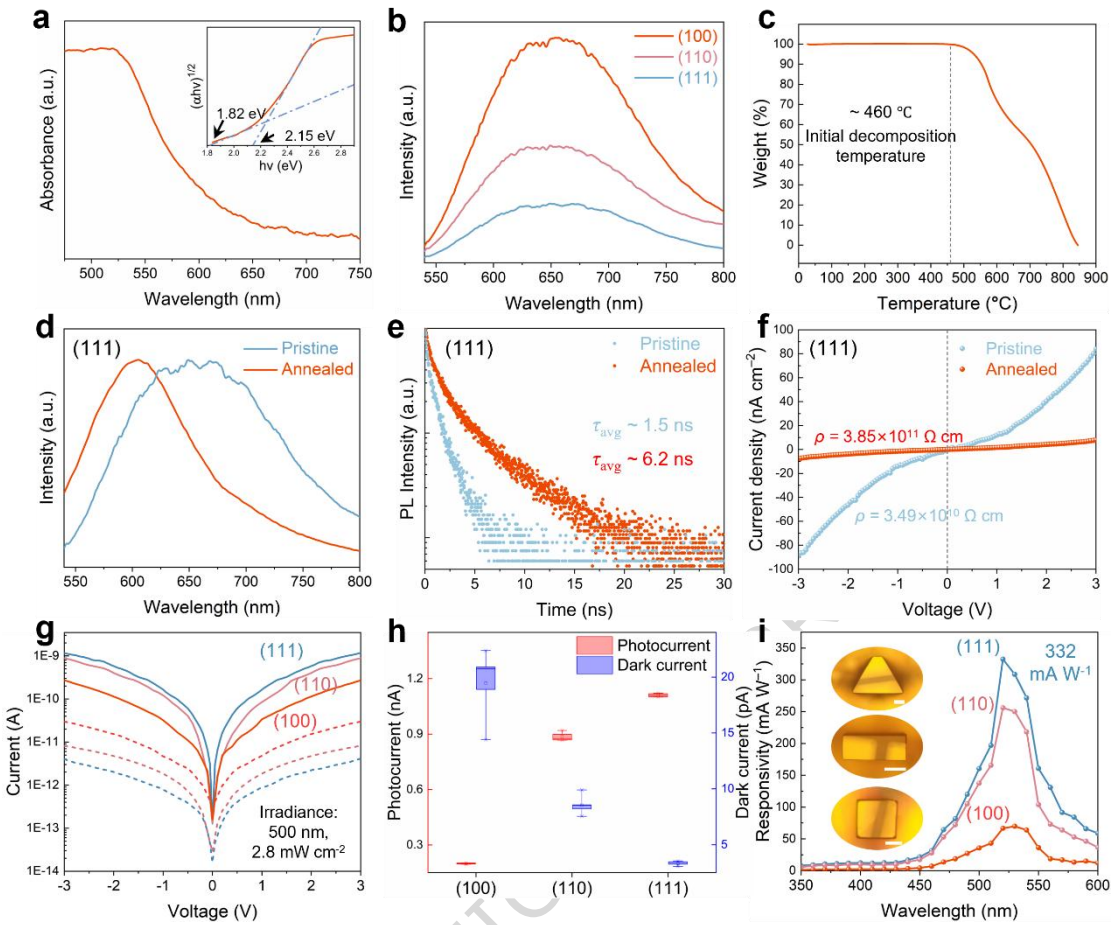

Fig. 5 | Optical, thermal, electronic and anisotropic optoelectronic properties of CABB PSCs. a, Absorption spectrum. Inset: Tauc-plot fitting curve, indicating the indirect phonon-assisted transition process. **b,** PL spectra collected from the surface of different facets. **c,** Thermogravimetric analysis curve, indicating the high decomposition temperature up to 460 °C. **d,** PL spectra of (111) facets before and after thermal annealing. **e,** Time-resolved PL spectra of (111) facets before and after annealing. **f,** Resistivity change of (111) facets before and after annealing. **g,** *I–V* curves of various facets in the dark state and under 500 nm light illumination (dashed line: dark current; solid lines: photocurrent). **h,** Statistical datasets of photo/dark currents of different crystal facets. The error bars represent the standard deviation and are calculated based on the variation in the currents, n = 5. **i,** Calculated responsivity of the (100), (110) and (111) facets as a function of wavelength from 350 to 600 nm, respectively. Inset: Optical images of the fabricated photodetectors. Scale bar: 50 μm.

Editorial Summary

Regulating the orientation of crystal facets is always an important but challenging issue. Here, the authors report the droplet interface synthesis of $Cs_2AgBiBr_6$ single crystals and the random (100)/(110)/(111) orientations can be transformed to a selective (111)-preferred orientation.

Peer review information: ***Nature Communications*** **thanks the anonymous reviewers for their contribution to the peer review of this work. A peer review file is available.**